Science
AAAS

# Supplementary Materials for

## Identification of single site gold catalysis in acetylene hydrochlorination

Grazia Malta, Simon A. Kondrat, Simon J. Freakley, Catherine J. Davies, Li Lu, Simon Dawson, Adam Thetford, Emma K. Gibson, David J. Morgan, Wilm Jones, Peter P. Wells, Peter Johnston, C. Richard A. Catlow, Christopher J. Kiely and Graham J. Hutchings*

*Corresponding author. E-mail: hutch@cf.ac.uk (G.J.H)

**This PDF file includes:**

## Materials and Methods

### Catalyst Preparation

A series of carbon-supported gold catalysts were prepared via a wet impregnation method. Activated carbon (Norit ROX 0.8) was initially ground to obtain a powder (100 - 140 mesh). The gold precursor $HAuCl_4 \cdot xH_2O$ (Alfa Aesar, 99.9% (metals basis), Au 49%, 40 mg) was dissolved in 5.4 mL of solvent: namely either (i) *aqua regia* (3 parts by volume [HCl (Fisher, 32 wt.%)]: 1 part by volume [$HNO_3$ (Fisher, 70 wt. %)]); or (ii) $HNO_3$ only (Fisher, 70 wt.%); or (iii) deionised water. The solutions of gold precursor were added drop-wise with stirring to the activated carbon (1.98 g). All the catalysts prepared had a nominal total metal loading of 1 wt.%. Stirring was continued at ambient temperature until $NO_x$ production subsided after ~1 h. The product was then dried for 16 h at 140 ºC under nitrogen flow. The catalysts prepared using *aqua regia*, $HNO_3$ or deionised water as solvents were labelled as Au/C-AR, Au/C-$HNO_3$ and Au/C-$H_2O$ respectively. It is important to note that this catalyst preparation method differs from those previously published (11), in that powdered carbon is used instead of extrudates. Consequently, the concentration of gold species will be significantly lower on the carbon surface when using powdered support. For comparative purposes, a 1 wt.% Au-thiosulfate/C catalyst (denoted Au/C-$S_2O_3$) was also prepared and tested. An aqueous $HAuCl_4$ solution was mixed with an aqueous solution of $Na_2S_2O_3$. The mixture obtained was added in aliquots to the activated carbon with mixing for a certain amount of time. The product was then dried at 110 °C overnight.

### Catalyst Testing

*In situ* XAFS measurements obtained under reaction conditions were performed in transmission mode using a fixed-bed polyimide (Kapton) microreactor (O.D. 6 mm, length 20 cm). Kapton possesses a unique combination of desirable physical properties, such as high chemical resistance, that are retained over a wide temperature range, and it does not give rise to significant X-ray attenuation.

The temperature was controlled with a Eurotherm controller with a type K thermocouple positioned in the centre of the heater block. The heater block, shown schematically below, was modified to allow the incident X-rays from the synchrotron to pass through the catalyst bed (Figure SE1).

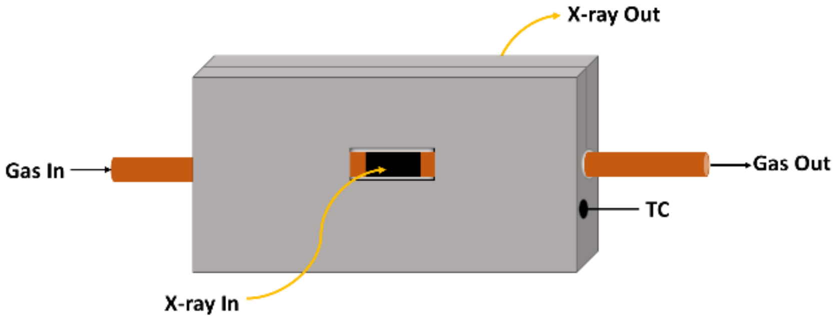

**Figure SE1.** Schematic diagram of the heater block used for the *in-situ* XAFS synchrotron experiment.For safety reasons, dilute gas mixtures were used. $C_2H_2$/Ar (4.91%

balanced in Ar, BOC) and HCl/Ar (5.00% balanced in Ar, BOC) gases were dried, using moisture traps, prior to introduction to the reactor. In all cases, the reactor was purged with Ar (99.99 % BIP, Air Products) prior to admitting the hydrochlorination reaction mixture. The reactor was heated to 200 °C at a ramp rate of 5 °C/min and held at temperature for 30 min, all under a flow of Ar. The reaction gas mixture of $C_2H_2$/Ar (24 mL $min^{-1}$), HCl/Ar (24 mL $min^{-1}$) and additional Ar (2 mL $min^{-1}$) was introduced into the heated reactor chamber containing catalyst (90 mg) at a total gas hourly space velocity (GHSV) of ~14,000 $h^{-1}$, keeping the $C_2H_2$ : HCl ratio at a constant value of 1 : 1.02. This residence time was chosen to test catalysts under mild conditions aiming for low conversion values in order to deliberately extend the catalyst induction period. Slightly different conditions were used for testing the Au/C-$S_2O_3$ material due to the different particle mesh size (>150 µm) of this catalyst, in order to avoid back pressure in the system. In this case, $C_2H_2$ (17.5 mL $min^{-1}$) and HCl (17.5 mL $min^{-1}$) were mixed via calibrated mass flow controllers into the heated reactor containing the catalyst (90 mg), to give a total flow rate of 35 mL $min^{-1}$ and a GHSV of ~11,000 $h^{-1}$.

The reaction mixture before and during the reaction was analysed on-line by mass spectrometry (Hiden QGA) equipped with a quartz inert capillary, that enabled both qualitative and quantitative analyses by scanning fixed mass fragments according to selected mass-to-charge ratios (m/z).

After mass spectroscopy analysis, the gas was passed through a bubbler containing aqueous sodium hydroxide solution in order to neutralise the unreacted hydrogen chloride (Figure SE2).

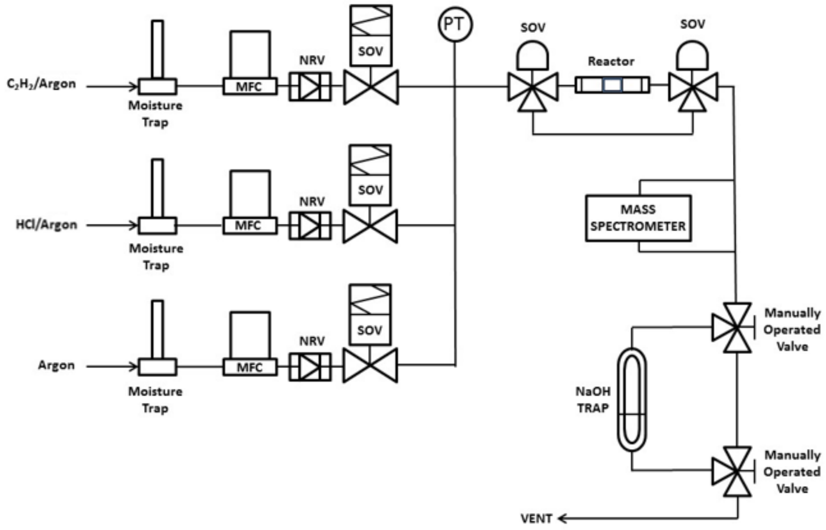

**Figure SE2.** Schematic diagram of the reaction set-up used for the *in-situ* XAFS synchrotron experiments. *Key;* MFC – mass flow controller, NRV – non-return valve, SOV – solenoid valve, PT – pressure transducer.

To be able to perform this *in situ* characterization, we used an automated reactor system. All the components were connected via a Process Interface unit (IGI Systems Ltd) equipped with a Eurotherm 3216 temperature controller and 230V AC solid state relay to power the heater block, a 16-bit analogue to digital convertor to acquire signal from the pressure transducer (to act as an over-pressure interlock for the gas flows) and an 8-channel electromechanical relay module to actuate each individual 2- and 3-way solenoid valve. The Process Interface unit also supplied 24V DC power and RS485 communication to the MFCs (Brooks Instrument GF40). All reaction parameter set points are controlled and adjusted remotely via LAB Interface software (IGI Systems Ltd) which also acts as process parameter monitor and data logger. The over-pressure interlock is fully automated.

The catalyst activity is shown in terms of productivity towards vinyl chloride monomer (VCM). We previously correlated the response factor of the mass spectrometer towards VCM with the productivity obtained by using a Varian 450 gas chromatograph equipped with a flame ionisation detector (FID). Chromatographic separation and identification of the products was carried out using a Porapak N packed column (6 ft × 1/8″ stainless steel). Using the correlation obtained between productivity and VCM mass spectrometer response it was possible to deduce the productivity for the reactions performed.

$$Productivity = \frac{(mol\ acetylene\ consumed * h^{-1})}{kg_{cat}}$$

## Catalyst Characterization

Powder X-ray diffraction (XRD) spectra were acquired using an X’Pert Pro PAN Analytical powder diffractometer employing a Cu $K_{\alpha}$ radiation source operating at 40 keV and 40 mA. Analyses of the spectra were carried out using X’Pert High Score Plus software. The crystallite size of the metallic gold nanoparticles, where possible, were determined using the Scherrer equation assuming a spherical particles shape and a K factor of 0.9 at the reflection arising from the set of {111} Au planes, at 2θ = 38°. Reflections due to metallic gold are expected to be present at 2θ angles of $38^{o}$ (111), $44^{o}$ (200), $64^{o}$ (220) and $78^{o}$ (311).

X-ray absorption fine structure (XAFS) spectra for all the Au/C samples were recorded at the Au $L_3$ absorption edge, in transmission mode, under reaction conditions, at the B18 beamline of Diamond Light Source, Harwell, UK. The measurements were performed using a QEXAFS setup with a fast-scanning Si (111) double crystal monochromator. For the *in situ* measurements the time resolution of the data acquisition was 20s/ spectrum.

The X-ray absorption near-edge structure (XANES) region of the XAFS spectrum is strongly sensitive to the chemistry of the absorbing atom. From XANES analysis it is possible to obtain information about the gold oxidation state and also to quantify the relative fractions of species with different oxidation states. In particular, we focused our attention on interpreting the magnitude of the rising absorption edge in the XANES region, typically called the ‘white line’. This feature corresponds to the Au $2p_{3/2} \rightarrow 5d$ primary transition, and it is detectable at an absorption energy of ~11920 eV. The intensity of the white line will therefore increase with an increase of oxidation state (*35*,*36*). By analysing the extended X-ray absorption fine structure (EXAFS) it is also possible to determine structural information, such as the bonding environment around the atom (*37*). Moreover, performing EXAFS data fitting allows one to determine the coordination number relative to the system analysed. The Demeter software package (Athena and Artemis) (*38,39*) was used for XAFS data analysis of both the Au and Cl data. Comparisons were made relative to a Au foil standard and $KAuCl_4$ and $AuCl_2^-$ standard compounds.

The Cl K-edge X-ray absorption spectra (XAS) have been measured to probe chloride-gold bonding. Spectra for the Au/C-AR samples at different time-on-line were recorded *ex situ* at the Cl K absorption edge in fluorescence mode, using beamline B18 of the Diamond Light Source, Harwell, UK. The measurements were performed using a QEXAFS setup with a fast-scanning Si (111) double crystal monochromator and a 36 element Ge fluorescence detector. The K-edge absorption spectrum of Cl when bound to a transition metal shows a pre-edge feature due to the forbidden 1s→3d transition. This transition becomes partially allowed and therefore observed when the Cl p-orbitals mix with the metal d-orbitals. The position of the pre-edge feature is dependent on several factors, namely (i) the Cl 1s energy, related to the charge on the chloride, and (ii) the metal d-orbital energy which is itself determined by both the oxidation state of the metal and the coordination number. The intensity of the pre-edge feature is dependent on the mixing of the Cl orbitals and metal d-orbitals and so the bonding characteristic of the Cl to the metal.

Materials for examination by scanning transmission electron microscopy (STEM) were dry dispersed onto a holey carbon TEM grid. These supported fragments were examined using BF- and HAADF-STEM imaging mode in an aberration corrected JEOL ARM-200CF scanning transmission electron microscope operating at 200kV. This microscope was also equipped with a Centurio silicon drift detector (SDD) system for X-ray energy dispersive spectroscopy (XEDS) analysis.

## Computational Details

All calculations were done using DFT using the CASTEP code (*40,41,42*). The PBE functional was used with dispersion correction using the Tkatchenko-Scheffler scheme (*43*). This scheme gave the best fit for the interlayer spacing in graphite with a spacing of 3.385 Å which is similar to the observed experimental value of 3.354 Å with a 0.9% difference (*44*). A planewave cut-off of 500 eV was applied and a single k-point at 0.25, 0.25, 0.25 was used with all calculations spin polarised. Charges on calculations are obtained from Hirshfeld population analysis unless otherwise stated, with Mulliken population analysis being the other method used.

The model used for the surface is from the work of Willock *et al* (*45)*. The carbon surface was made by cutting bulk graphite along the (119) plane producing a vicinal surface containing a step edge. The surface was stabilised with the addition of dissociated water molecules with either a hydroxyl group or hydrogen atom on each two-coordinate carbon atom, which stabilises the surface by 316 kJ mol$^{-1}$ per molecule. Dissociated HCl used in replacement of water has the effect of stabilising the surface by 307 kJ mol$^{-1}$ per molecule. This would indicate that there would be the mix and hydroxyl groups, chlorides and protons on the step-edge. However, for the purposes of this study the hydroxylated surface was the only one considered due to the reaction proceeding under acidic conditions, which served to simplify the model.

AuCl and $AuCl_3$ were absorbed onto the surface at several locations. The AuCl tends to favour the carbon atoms associated with the step edge. The site that is most favoured has a hydrogen atom attached to the step-edge carbon atom with a binding energy of -199 kJ $mol^{-1}$. This should be compared to $AuCl_3$, which binds to both the carbon on the step edge and to the hydroxyl groups on the step edge with binding energies of -323 kJ $mol^{-1}$ and -318 kJ $mol^{-1}$ respectively. In addition, an isolated Au atom has a binding energy of -96 kJ $mol^{-1}$ on the flat plateau slightly away from the step edge. When the charges are compared, all systems show a reduction in the magnitude of the Au charge from the isolated molecule. $AuCl_3$ shows about 3 times the charge compared to AuCl in the gas phase, which is most clearly shown in the magnitude of their Mulliken charges (0.74e and 0.28e respectively) and Hirshfeld charges (0.41e and 0.19e respectively).

**Figure S1.**

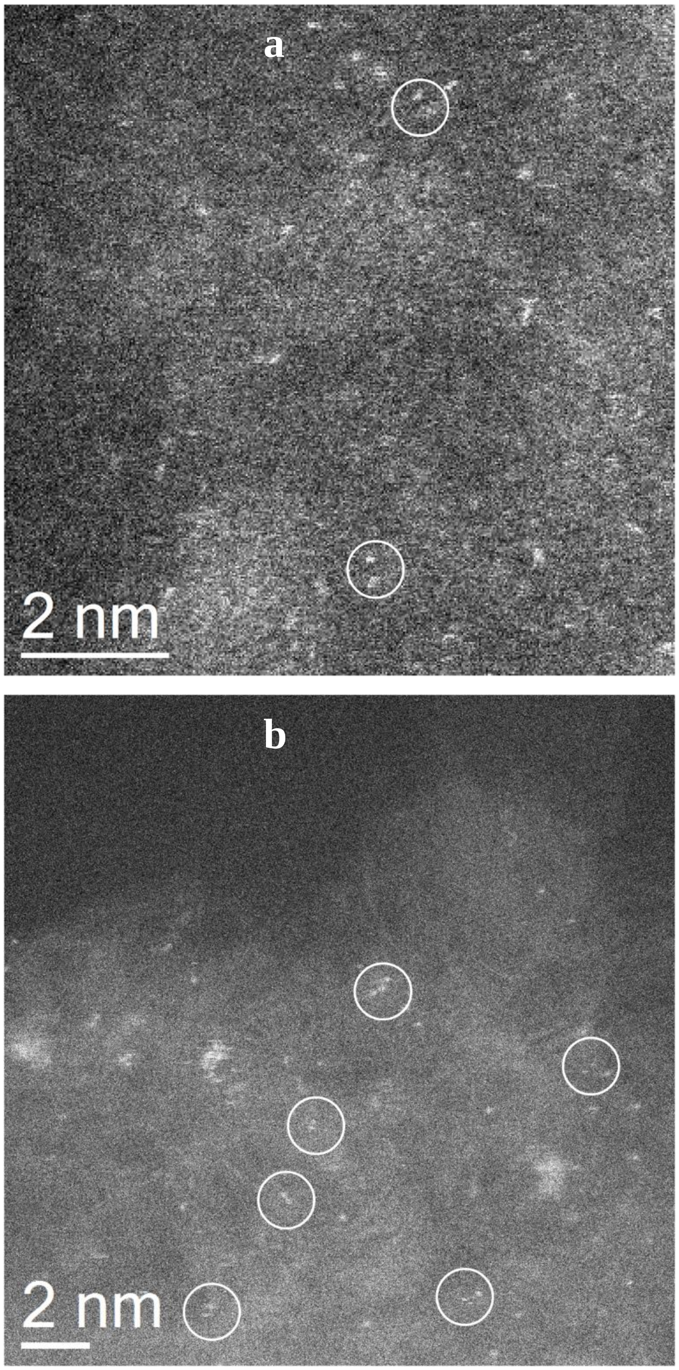

Representative STEM-HAADF image of the Au/C-AR catalyst in (**a**) the unused state and (**b**) the used state showing the presence of occasional Au dimers (circled) as well as atomically dispersed Au species. The projected separations of Au atoms in the dimeric species were typically in the 0.2.-0.34 nm range, which is below the 0.34 nm Au-Au separation found in $AuCl_3$.

**Figure S2.**

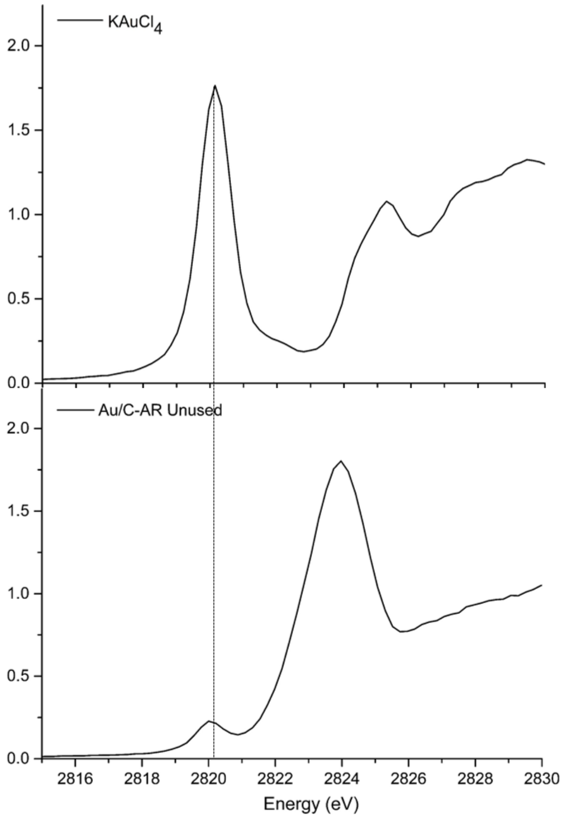

*Ex-situ* Cl K-edge XANES for the 1 wt% Au/C-AR catalyst in the unused state compared to $KAuCl_4$ (standard material for the Cl-Au bond).

**Figure S3.**

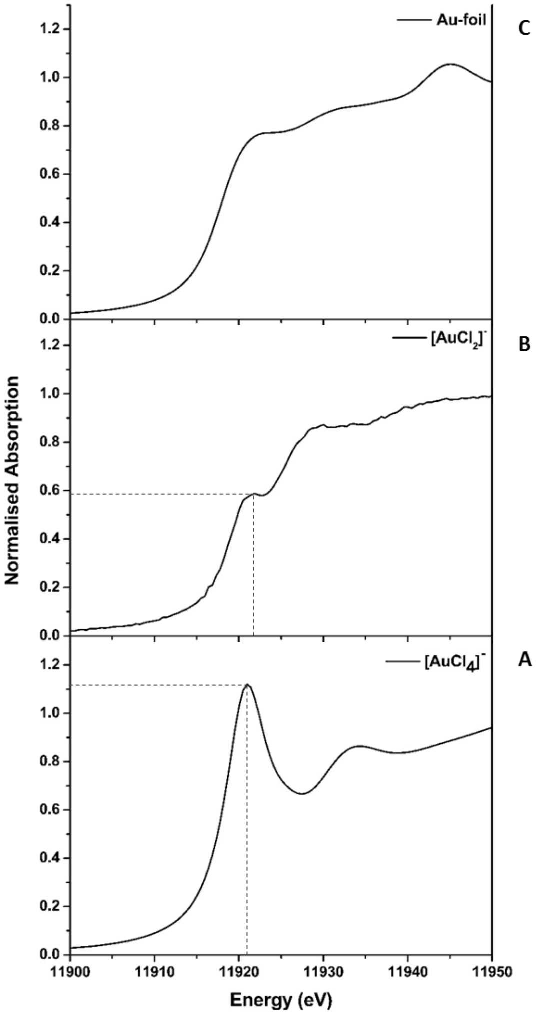

Au $L_3$-edge XANES region for the Au standards used: (A) Au(III) [AuCl$_4$]$^-$, (B) Au(I) [AuCl$_2^-$] and (C) Au$^0$ gold foil. For the two cationic Au standards, the white line intensity values are ~ 1.1 and ~ 0.6 respectively.

In the XANES region of the Au(III) standard spectrum (**A**) a very prominent feature on the absorption edge is observed and this is attributed to the Au $2p_{3/2} \rightarrow 5d$ transition. The intensity of this peak is reduced in the Au$^+$ standard (**B**) and is absent for the Au$^0$ foil (**C**). In all cases, we show a normalized edge step, so that the values of the normalized absorption are between 0 and 1.2.

**Figure S4.**

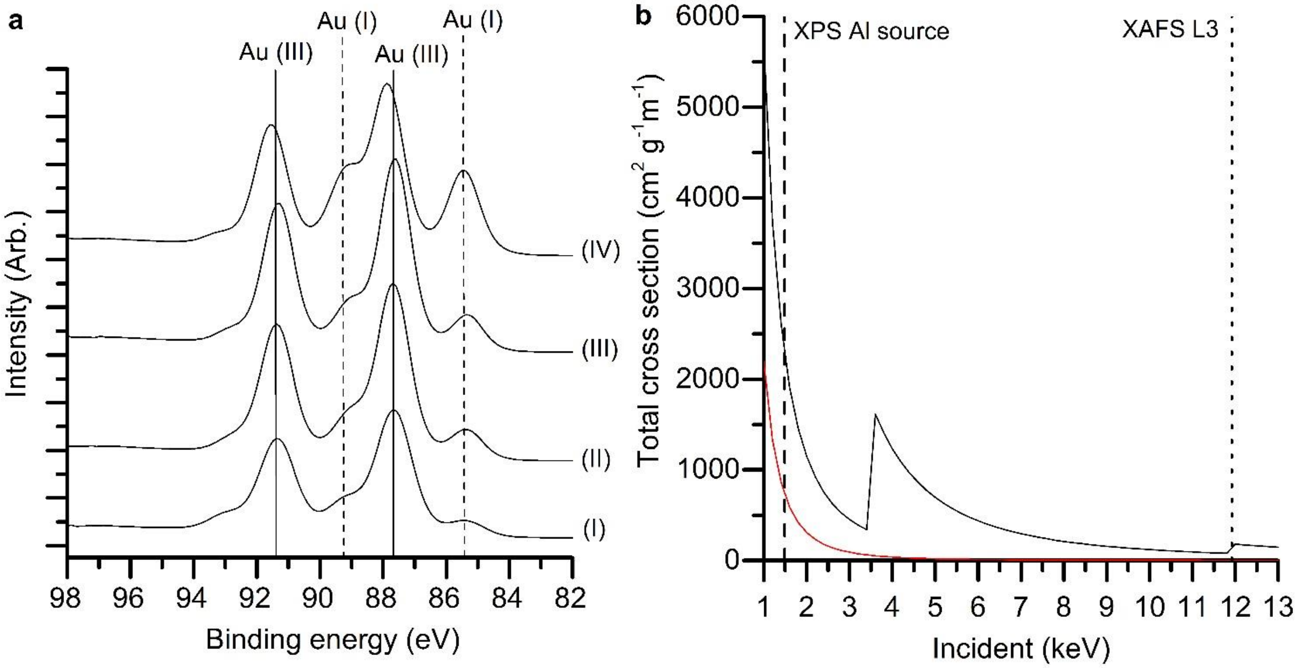

Photo-reduction of gold chloride species during under X-ray illumination. (a) Photo-reduction of $KAuCl_4$ during Au(4f) XPS analysis for increasing X-ray exposure time (approximately 50 s per Au(4f) spectra). (b) X-ray absorption cross-section with respect to incident energy for Au (black line) and C (red line).

The initial XPS spectra of $KAuCl_4$ (Figure S4a) shows the expected dominant species is Au(III) at 87.6 eV, with a small signal at 85.4 eV that can be assigned as Au(I). Subsequent scans show that the Au (I) contribution steadily increases at the expense of the Au(III) signal. This is clear evidence of X-ray induced reduction of Au(III) in $KAuCl_4$, which is in agreement with previous studies (*46, 47*), and highlights the issues of characterising cationic Au species by XPS. Metallic Au, which is frequently observed in Au/C acetylene hydrochlorination catalysts by XPS analysis must be considered with caution. It is likely that the photo-reduction phenomena observed for the $KAuCl_4$ would be much more pronounced for isolated $AuCl_x$ species supported on a reducing carbon support. We therefore conclude that XPS analysis of Au/C acetylene hydrochlorination catalysts substantially over estimates the contribution of metallic Au, due to the rapid photo-reduction of dispersed cationic $AuCl_x$ species.

The absence of this photo-reduction phenomenon during XAFS analysis at first sight seems to be counter-intuitive, as this technique also subjects the sample to an X-ray beam, but with an incident energy of *ca.* 11.9 keV as compared to an Al source XPS incident energy of 1.487 keV. However, the difference in photo-reduction rates for the two processes can be explained when the probability of photon absorption as a function of incident energy is considered (Figure S4b). The cross-section for an Au absorber is an order of magnitude greater at XPS incident energies (2275 $cm^2g^{-1}m^{-1}$) as compared to $L_3$ edge XAFS incident energies (182 $cm^2g^{-1}m^{-1}$). Given that the X-ray flux of both techniques is *ca.* $1E^{11}$ ph $s^{-1}$, the probability of the incident X-ray interacting with matter is an order of magnitude greater with XPS. In addition, the absorption cross-section for the C support is considerably more significant at lower incident energies.  In conjunction with the reduced absorption cross-section during XAFS experiments, X-ray penetration into the bulk of the sample will limit the relative number of escaping hot electrons.

**Figure S5.**

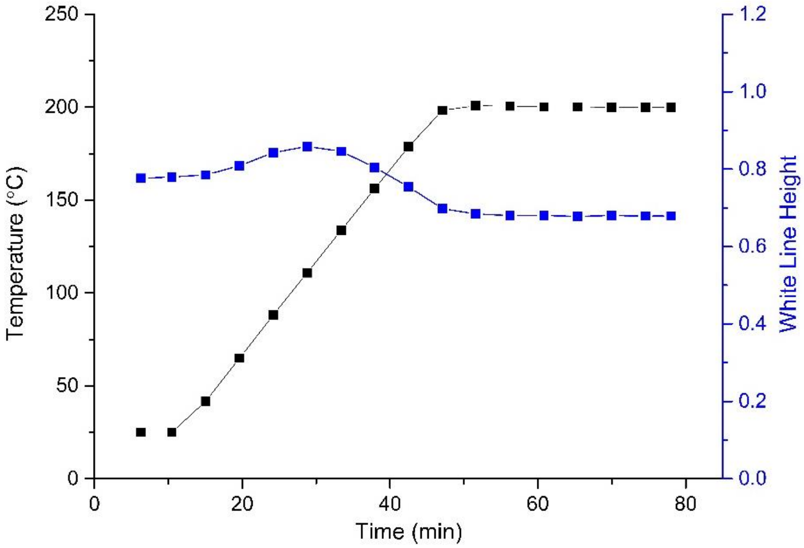

Au $L_3$-edge XANES for the 1% Au/C-AR catalyst during heating to reaction temperature under Ar at 5 °C $min^{-1}$.

**Figure S6.**

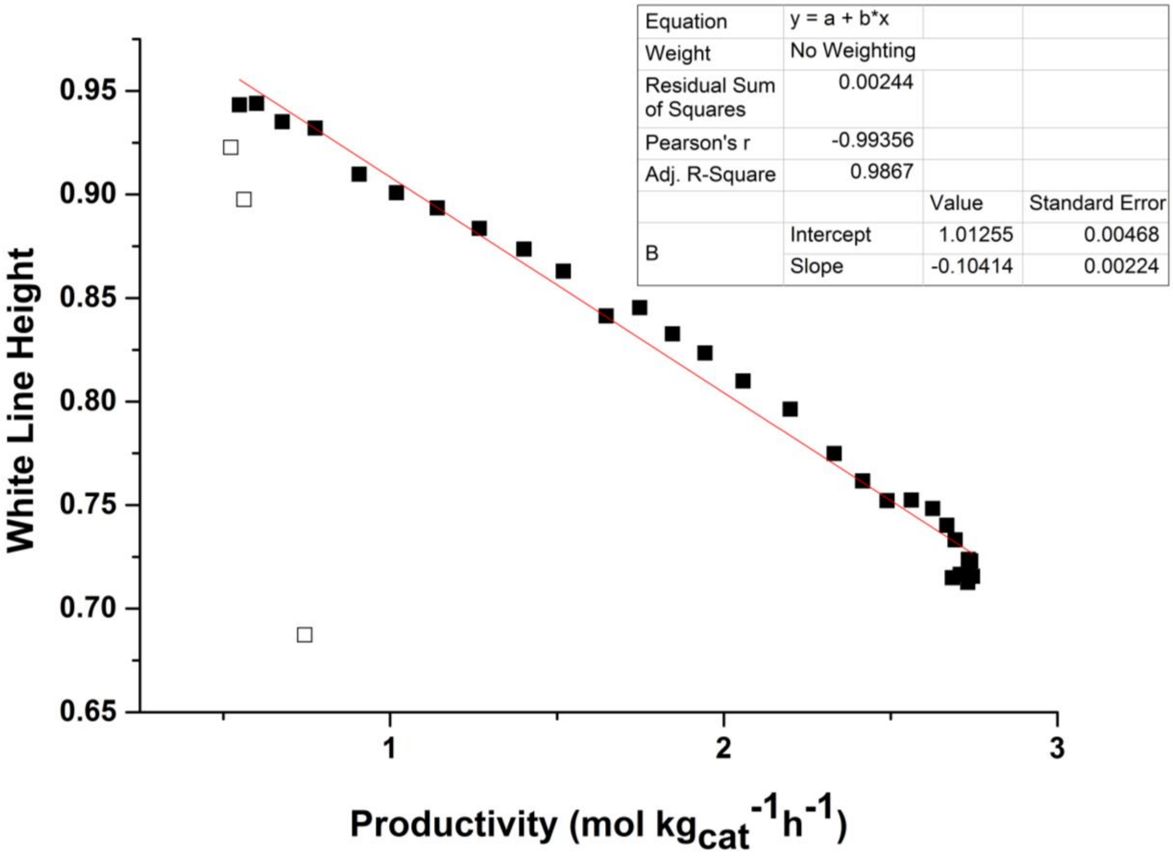

| | | | |
|---|---|---|---|
| Equation | y = a + b*x | | |
| Weight | No Weighting | | |
| Residual Sum of Squares | 0.00244 | | |
| Pearson's r | -0.99356 | | |
| Adj. R-Square | 0.9867 | | |
| | | Value | Standard Error |
| B | Intercept | 1.01255 | 0.00468 |
| | Slope | -0.10414 | 0.00224 |

Plot of VCM productivity and the corresponding normalized Au $L_3$ edge white –line intensity for the 1wt% Au/C-AR catalyst during the 240 min time-on-ine. Open squares denote data acquired during the first 15 min of the reaction while closed squares for data points collected between 15 and 240 min time-on-line

**Figure S7.**

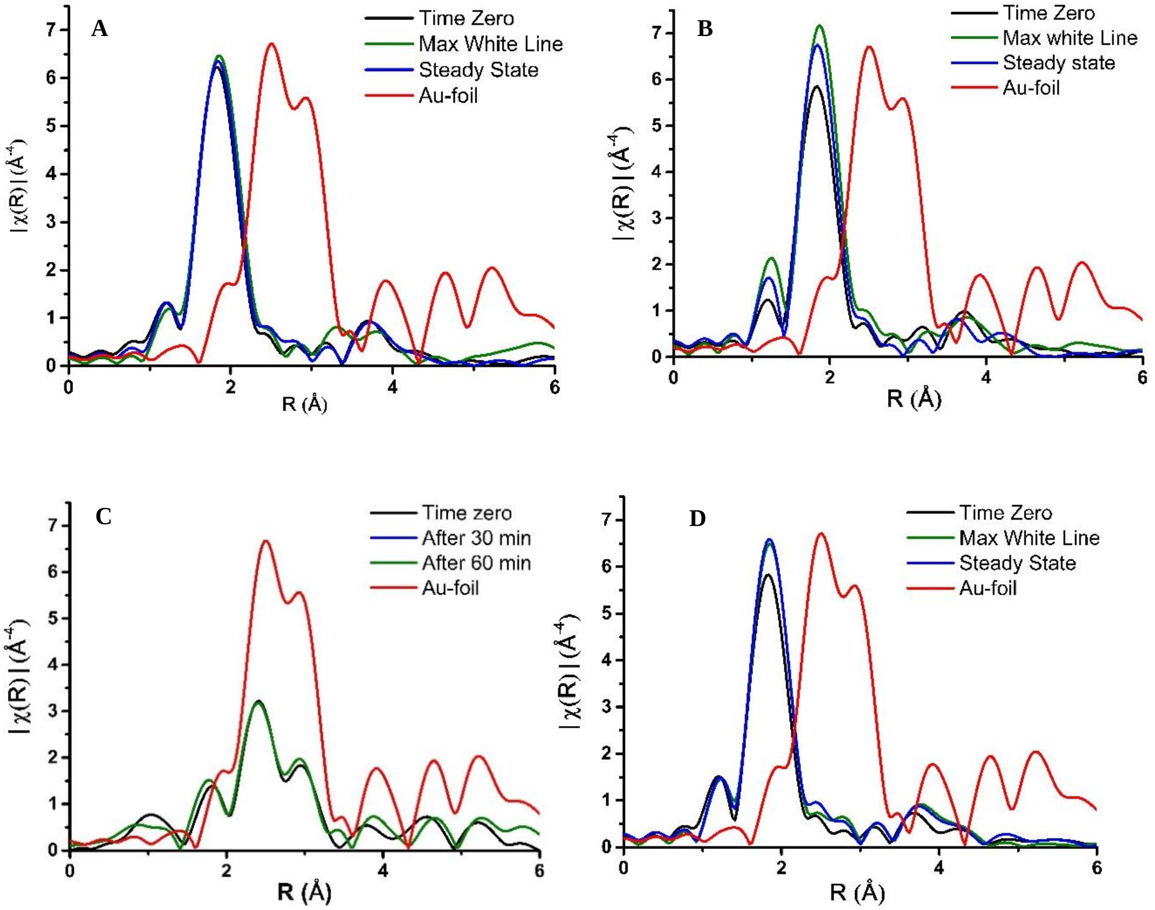

EXAFS data of the Au $L_3$- edge under reaction conditions for the (**A**) 1 wt.% Au/C-AR, (**B**) 1 wt.% Au/C-$HNO_3$, (**C**) 1 wt.% Au/C-$H_2O$ and (**D**) 1 wt.% Au/C-$S_2O_3$ catalyst materials at different times-on-line. *Reaction conditions:* T = 200 °C, $C_2H_2$:HCl = 1:1.02, GHSV (total) = 14000 $h^{-1}$ or 11000 $h^{-1}$ for the Au/C-$S_2O_3$ catalyst.

**Figure S8.**

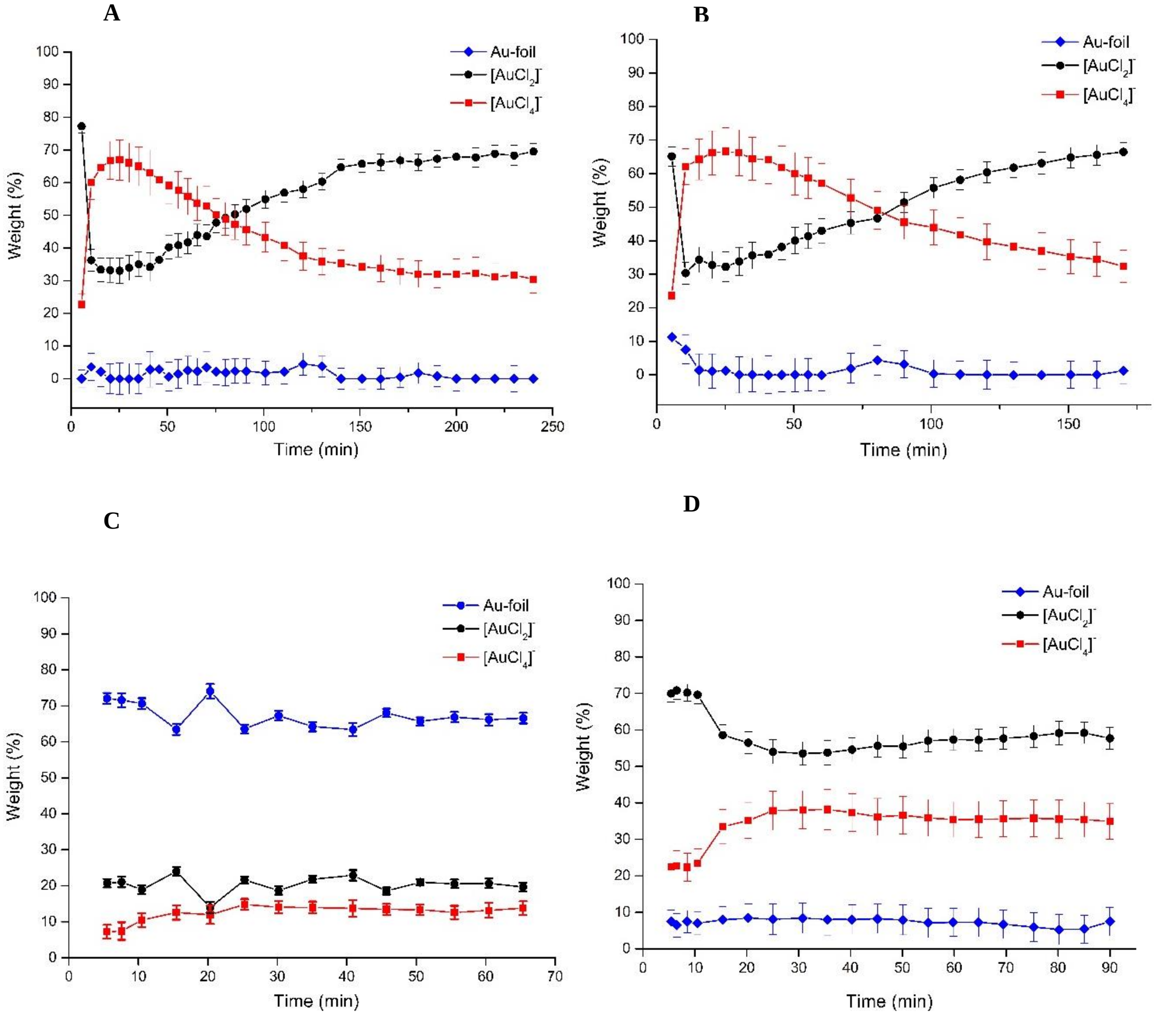

Linear combination fitting of the XANES data under reaction conditions for (**A**) 1 wt.% Au/C-AR, (**B**) 1 wt.% Au/C-HNO$_3$, (**C**) 1 wt.% Au/C-H$_2$O and (**D**) 1 wt.% Au/C-S$_2$O$_3$ catalyst sample materials. *Reaction conditions:* T = 200 °C, $C_2H_2$ : HCl = 1 : 1.02, GHSV (total) = 14,000 h$^{-1}$ or 11,000 h$^{-1}$ for the Au/C-S$_2$O$_3$ catalyst.

**Figure S9.**

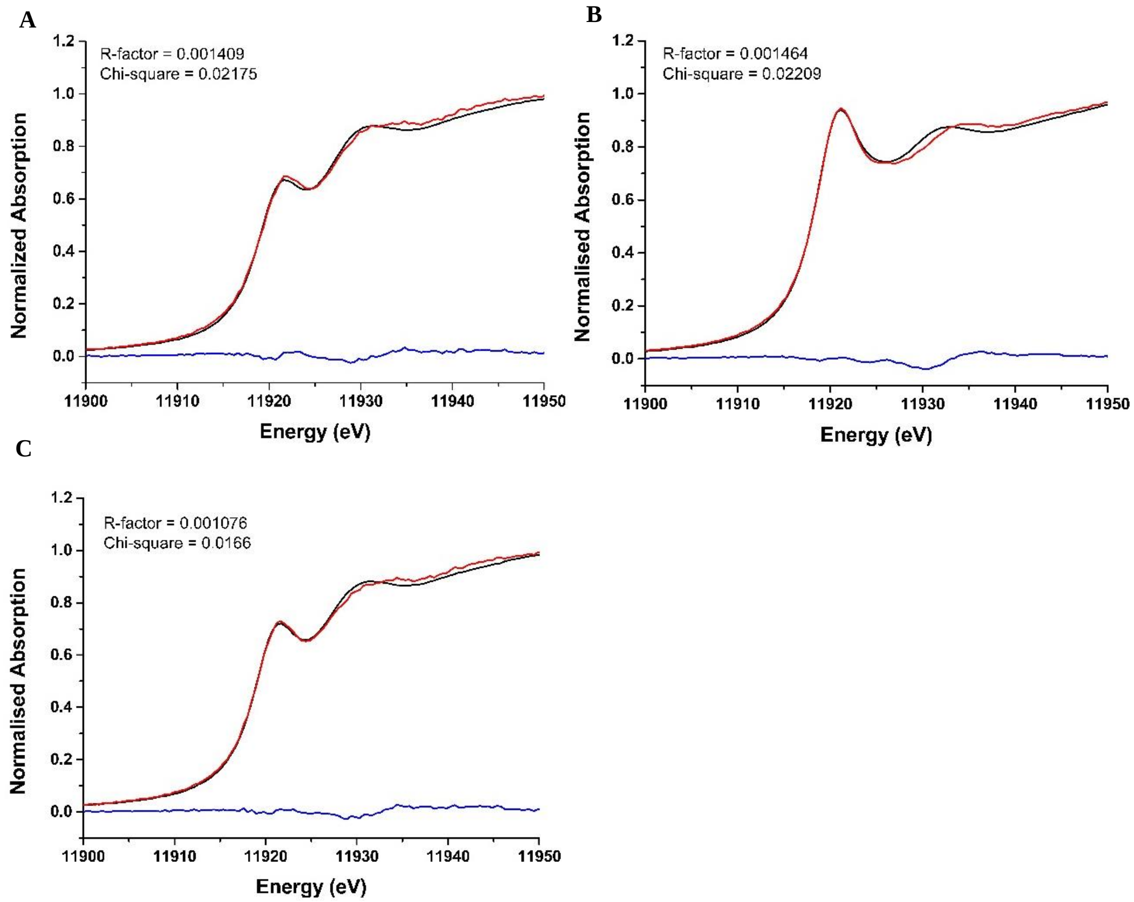

XANES data fitting for the 1 wt% Au/C-AR catalyst under reaction conditions at three different points in the induction cycle: (**A**) time zero, (**B**) maximum of the white line intensity and (**C**) steady state. *Key:* black line (experimental data); red line (fit); blue line (residual). *Reaction conditions:* T = 200 °C, $C_2H_2$ : HCl = 1 : 1.02, GHSV (total) = 14,000 $h^{-1}$.

**Figure S10.**

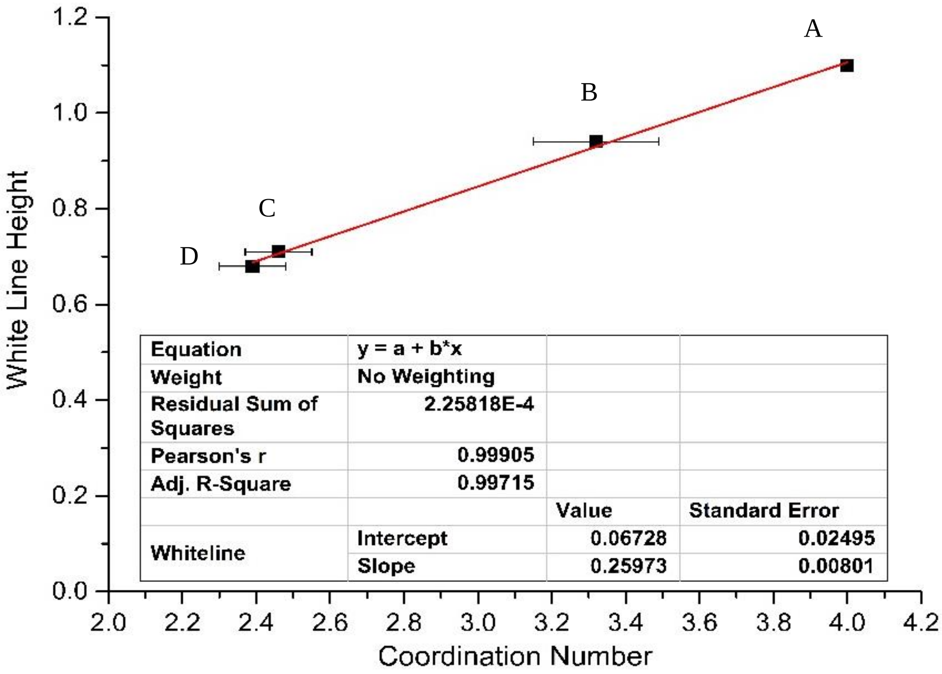

| | | | |
|---|---|---|---|
| Equation | y = a + b*x | | |
| Weight | No Weighting | | |
| Residual Sum of Squares | 2.25818E-4 | | |
| Pearson's r | 0.99905 | | |
| Adj. R-Square | 0.99715 | | |
| | | Value | Standard Error |
| Whiteline | Intercept | 0.06728 | 0.02495 |
| | Slope | 0.25973 | 0.00801 |

Correlation of relative Au $L_3$ white line intensity with Au coordination number for the 1 wt.% Au/C-AR catalyst under reaction conditions corresponding to figure 2A in the main paper: (**A**) the Au(III) ($KAuCl_4$) standard, at (**B**) the maximum of the white line intensity, after ca. 25 min of reaction, at (**C**) steady state (after 240 min of reaction) and at (**D**) corresponding to time zero (beginning of reaction). *Reaction conditions:* T = 200 °C, $C_2H_2$ : HCl = 1 : 1.02, GHSV (total) = 14,000 $h^{-1}$.

**Figure S11.**

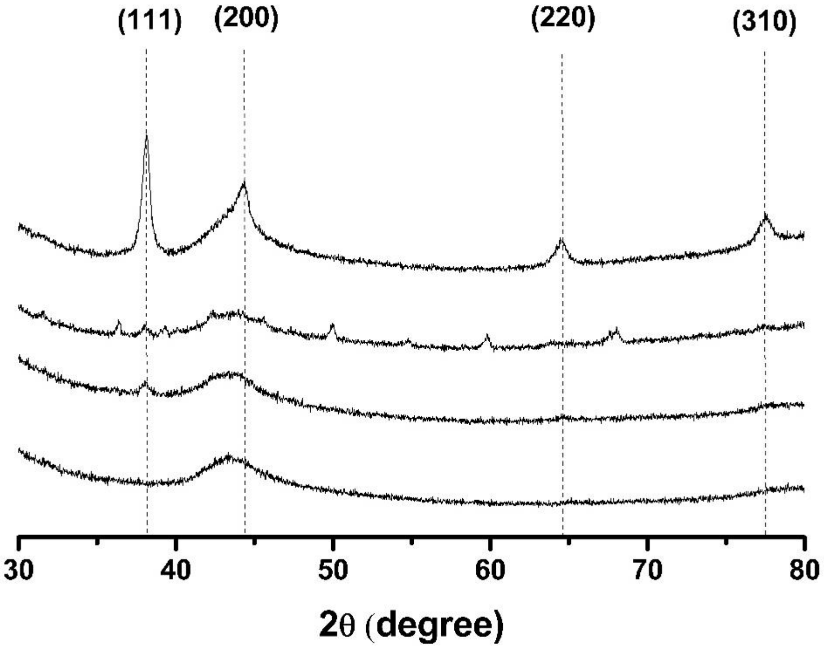

X-ray powder diffraction patterns of the (A) 1 wt.% Au/C-AR, (B) 1 wt.% Au/C-$HNO_3$, (C) 1 wt.% Au/C-$S_2O_3$, and (D) 1 wt.% Au /C-$H_2O$ catalyst materials before use.

Note that no distinct f.c.c. gold reflections were observed in the 1 wt% Au/C-AR catalyst (**A**). A weak broad (111) Au reflection ($2\theta = 38^o$) was observed for the 1 wt% Au/C-$HNO_3$ and 1 wt% Au/C-$S_2O_3$ catalysts (**B, C**). For the 1 wt% Au /C-$H_2O$ catalyst (**D**), reflections corresponding to (111), (200), (220 and (310) Au lattice planes were clearly visible suggesting the presence of numerous discrete Au nanoparticles. Scherrer analysis of the (111) reflections of this latter material gave an estimated crystallite size of 17 nm. The undefined reflections observed for the (**C**) Au/C-$S_2O_3$ catalyst can be attributed to quartz compound present as an impurity in the support.

**Figure S12.**

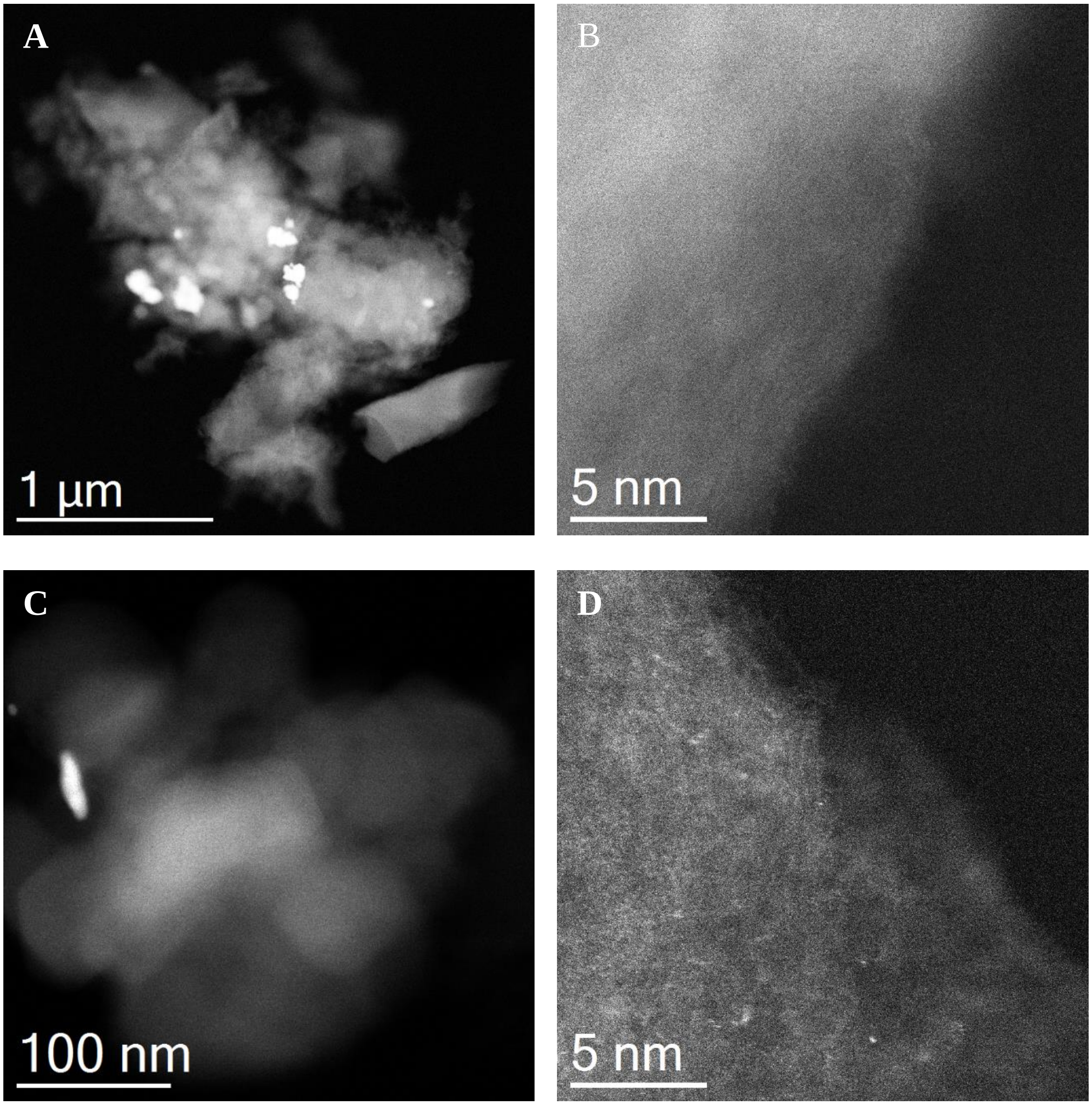

Representative STEM-HAADF images of the Au/C-$H_2O$ catalyst in (**A, B**) the unused and (**C, D**) used states.

Prior to use this catalyst consist entirely of supported gold nanoparticles in the 5-100 nm size range (**A**). The carbon support areas were totally devoid of any atomically dispersed species (**B**). After use the 5-100 nm particles were still evident (**C**), but now there was evidence of some very occasional atomically dispersed Au entities in the carbon support (**D**).

**Figure S13.**

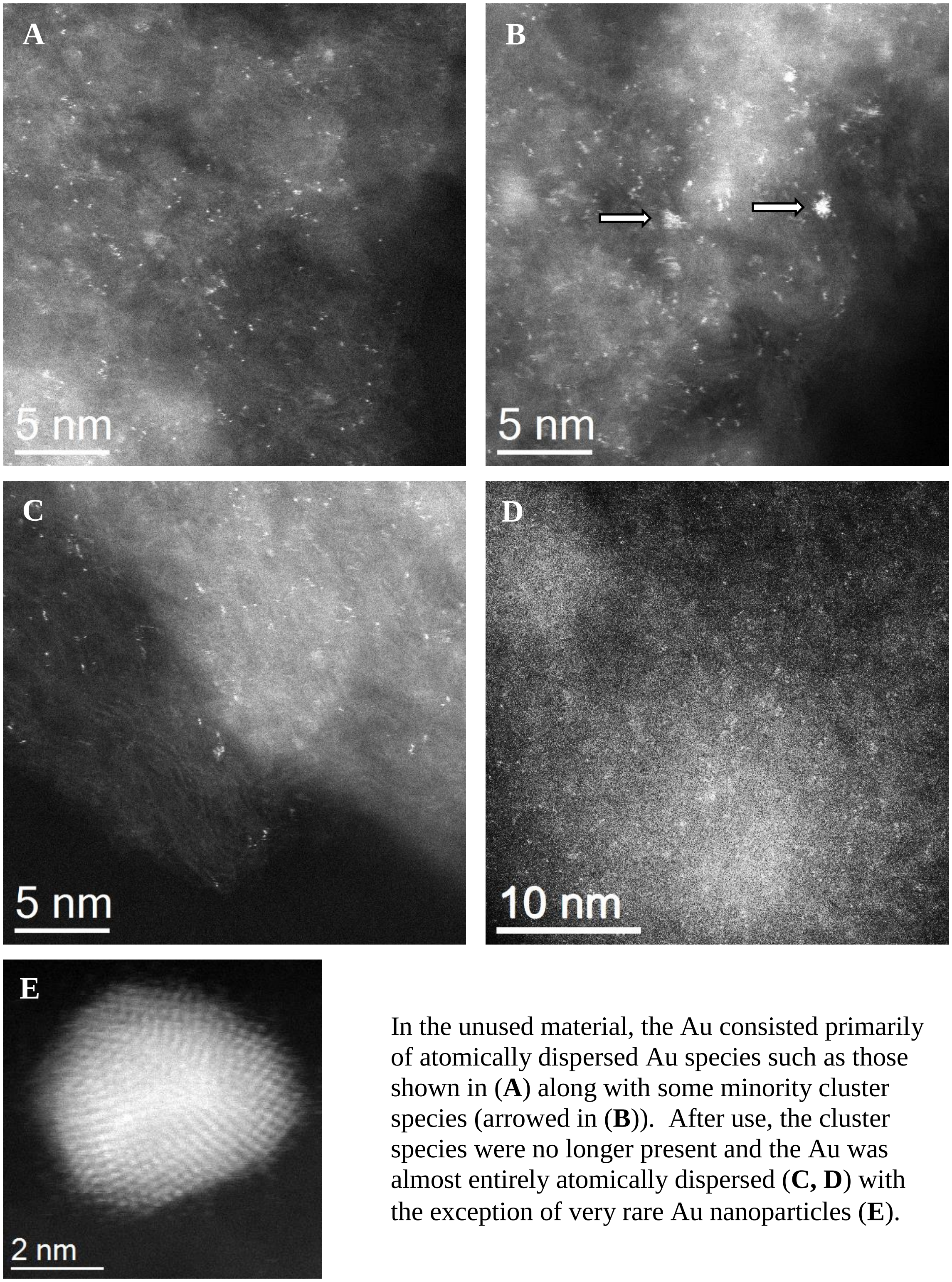

In the unused material, the Au consisted primarily of atomically dispersed Au species such as those shown in (**A**) along with some minority cluster species (arrowed in (**B**)). After use, the cluster species were no longer present and the Au was almost entirely atomically dispersed (**C, D**) with the exception of very rare Au nanoparticles (**E**).

Representative STEM-HAADF images of the Au/C-$S_2O_3$ catalyst in (**A, B**) the unused and (**C, D, E**) used states.

## Table S1

EXAFS modelling for the Au L3-edge of the KAuCl$_4$ standard, Au/C-AR (fresh and *in-situ*) and Au/C-S$_2$O$_3$ (fresh and *in-situ*) samples at different times-on-line.

| **Sample** | **Scattering path** | **CN** | **R (Å)** | **$2\sigma^2$ (Å$^2$)** | **So2** | **$E_f$ (eV)** | **$R_{factor}$** |
|---|---|---|---|---|---|---|---|
| **KAuCl$_4$ (Au$^{3+}$ std)** | Au-Cl1 | 4* | 2.284(3) | 0.001 | 0.75(3) | 2.9(5) | 0.014 |
| **Au/C-AR unused** | Au-Cl1 | 2.58(8) | 2.273(4) | | | 2.8(7) | 0.006 |
| **Au/C-AR**<br>**0 min**<br>***in situ*** | Au-Cl1 | 2.39(9) | 2.268(6) | 0.0037[#] | | 1(1) | 0.008 |
| **Au/C-AR^**<br>**20 min**<br>***in situ*** | Au-Cl1 | 2.78(46) | 2.297(18) | | | 1(1) | 0.005 |
| | Au-Cl2 | 0.54(37) | 2.171(76) | | | | 0.005 |
| | Combined | 3.32(83) | 2.277 | | | | - |
| **Au/C-AR**<br>**240 min**<br>***in situ*** | Au-Cl1 | 2.46(9) | 2.275(6) | | | 1.2(9) | 0.006 |
| **Au/C-S$_2$O$_3$ unused** | Au-S(Cl)[$] | 1.97(8) | 2.269(5) | 0.001 | | 1.7(9) | 0.010 |
| **Au/C-S$_2$O$_3$**<br>**0 min*in situ*** | Au-S(Cl)[$] | 2.23(6) | 2.264(7) | 0.0037[#] | | 1.3(6) | 0.005 |
| **Au/C-S$_2$O$_3$**<br>**30 min**<br>***in situ*** | Au-S(Cl)[$] | 2.61(9) | 2.277(5) | | | 2.0(8) | 0.007 |

* KAuCl$_4$ standard was fitted with a fixed CN of 4 and used to determine the Debye-Waller factor (for samples at 25 ˚C) and also the amplitude reduction factor for all other fittings.

[#] Debye-Waller factor at 200 ˚C was calculated from literature values and the value calculated at 25 ˚C.

[$] Due to comparable Z numbers, S and Cl are indistinguishable via EXAFS analysis.

^ For the Au/C-AR catalyst after 20 min reaction time, two distinct Au-Cl scattering paths were observed.

**Table S2.**

LC-XANES results and fitting parameters.

| **Sample** | | **Quantification (%)** | | | **R factor** | **$\Delta E^0$** | | |
|---|---|---|---|---|---|---|---|---|
| | | **$Au^0$** | **$Au^+$** | **$Au^{3+}$** | | **$Au^0$** | **$Au^+$** | **$Au^{3+}$** |
| **Au/C-AR** | **Unused** | 0 (3.5) | 55.7 (2.7) | 44.3 (4.4) | 0.001150 | - | 0.70 (0.07) | 0.25 (0.05) |
| | **Time zero** | 0 (3.3) | 75.2 (2.5) | 24.8 (4.0) | 0.001409 | - | 0.63 (0.05) | 0.20 (0.09) |
| | **Maximum of the white line intensity** | 0 (4.8) | 33.1 (3.9) | 66.9(6.1) | 0.001464 | - | -1.23 (0.13) | 0.80 (0.05) |
| | **Steady State** | 0 (4.05) | 68.3 (3.05) | 31.7 (5.1) | 0.001076 | - | 0.55 (0.07) | 0.33 (0.08) |
| **Au/C-$HNO_3$** | **Unused** | 2.0 (3.9) | 64.6 (2.9) | 33.4 (4.8) | 0.001266 | - | 0.64 (0.07) | 0.49 (0.07) |
| | **Time zero** | 10.7 (3.8) | 65.6 (2.8) | 23.7 (4.7) | 0.001242 | - | 0.8 (0.07) | 0.7 (0.1) |
| | **Maximum of the white line intensity** | 0 (5.4) | 33.8 (4.2) | 66.2 (6.9) | 0.001797 | - | -0.5 (0.15) | 0.9 (0.05) |
| | **Steady State** | 1.2 (3.8) | 66.5 (2.8) | 32.3 (4.8) | 0.001196 | - | 0.6 (0.07) | 0.5 (0.07) |
| **Au/C-$S_2O_3$** | **Unused** | 4.9 (3.4) | 71.9 (2.6) | 23.1 (4.4) | 0.000952 | - | 0.43 (0.054) | 0.60 (0.09) |
| | **Time zero** | 7.5 (3.04) | 70.00 (2.32) | 22.5 (3.83) | 0.000777 | - | 0.42 (0.05) | 0.30 (0.09) |
| | **Minimum of the white line intensity** | 6.45 (3.27) | 70.80 (2.46) | 22.7 (4.09) | 0.000882 | - | 0.53 (0.053) | 0.40 (0.090) |
| | **Maximum of the white line intensity** | 8.40 (4.13) | 53.50 (3.21) | 38.10 (5.23) | 0.001321 | - | 0.05 (0.08) | 0.52 (0.070) |
| | **Steady State** | 7.4 (3.9) | 57.70 (2.9) | 34.9 (4.9) | 0.001216 | - | 0.40 (0.075) | 0.54 (0.070) |
| **Au/C-$H_2O$** | **Unused** | 72.5 (2.7) | 22.2 (2.1) | 5.4 (3.5) | 0.000412 | - | -1.52 (0.10) | 1.42 (0.31) |
| | **Time zero** | 70.00 (1.7) | 22.3 (1.4) | 7.7 (2.2) | 0.000122 | - | -1.5 (0.06) | 1.3 (0.14) |
| | **After 10 minutes of reaction** | 71.60 (1.9) | 21.01 (1.50) | 7.40 (2.42) | 0.000129 | - | -1.30 (0.07) | 1.42 (0.150) |
| | **After 30 minutes of reaction** | 74.05 (2.03) | 13.99 (1.55) | 11.96 (2.56) | 0.000108 | - | 0.12 (0.15) | 0.80 (0.11) |
| | **After 65 minutes of reaction** | 66.9 (1.43) | 20.6 (1.15) | 12.7 (1.84) | 0.000126 | - | -1.95 (0.07) | 1.04 (0.08) |

---

1. P. Johnston, N. Carthey, G. J. Hutchings, *J. Am. Chem. Soc.* **137**, 14548-14557 (2015).
2. R. Ciriminna, E. Falletta, C. Della Pina, J. H. Teles, M. Pagliaro, *Angew. Chem. Int. Ed.*, 55,14210 –14217 (20016).
3. G. J. Hutchings, *J. Catal.* **96**, 292-295 (1985).
4. B. Nkosi, N. J. Coville, G. J. Hutchings, *Appl. Catal.* **43**, 33-39 (1988).
5. http://www.mercuryconvention.org/.
6. B. Nkosi *et al.*, *J. Catal.* **128**, 366-377 (1991).
7. G. Hong *et al.*, *RSC Adv.* **6**, 3806-3814 (2016).
8. M. Zhu *et al.*, *ACS Catal.* **5**, 5306-5316 (2015).
9. X. Tian *et al.*, *RSC Adv.* **5**, 46366-46371 (2015).
10. B. Nkosi, M. D. Adams, N. J. Coville, G. J. Hutchings, *J. Catal.* **128**, 378-386 (1991).
11. X. Liu *et al.*, *Catal. Sci. Tech.* **6**, 5144-5153 (2016).
12. S. Carrettin *et al., Adv. Synth. Catal.* **348**, 1283-1288 (2006).
13. L. Huang *et al*., *Angwe. Chem, Int, Ed.* **55**, 4808-4813 (2016).
14. A. S. K. Hashmi, *Gold Bulletin.* **36**, 3-9 (2003).
15. M. Flytzani-Stephanopoulos, *Acc. Chem. Res.***47**, 783-792 (2014).
16. W. Deng, A. I. Frenkel, R. Si, M. Flytzani-Stephanopoulos, *J. Phys. Chem. C* **112**, 12834-12840 (2008).
17. J. C. Fierro-Gonzalez, B. C. Gates, *J. Phys. Chem. B.* **108**, 16999-17002 (2004).
18. J. Lu, C. Aydin, N. D. Browning, B. C. Gates, *Angew. Chem., Int. Ed.* **51**, 5842-5846 (2012).
19. M. C. Blanco Jaimes, C. R. N. Böhling, J. M. Serrano-Becerra, A. S. K. Hashmi, *Angew. Chem., Int. Ed.* **52**, 7963-7966 (2013).
20. M. C. Blanco Jaimes *et al.*, *Chem. Commun.* **50**, 4937-4940 (2014).
21. A. S. K. Hashmi *et al.*, *Chem. - Eur. J.* **16**, 8012-8019 (2010).
22. Supporting information is avaliable online (Experimental details, Tables S1-2, Figures S1 – 13, and references 32-44)
23. S.-Y. Chang *et al.*, *RSC Adv.* **5**, 6912-6918 (2015).
24. A. Pantelouris, G. Kueper, J. Hormes, C. Feldmann, M. Jansen, *J. Am. Chem. Soc.* **117**, 11749-11753 (1995).
25. I. Berrodier *et al.*, *Geochim. Cosmochim. Acta* **68**, 3019-3042 (2004).
26. O. Glemser, H. Sauer, Handbook of Preparative Inorganic Chemistry. *Academic Press* **2**, 1056 (1965).
27. P. Hu, P. N. Duchesne, Y. Song, P. Zhang, S. Chen, *Langmuir* **31**, 522-528 (2015).
28. N. Weiher *et al.*, *J. Am. Chem. Soc.* **129**, 2240-2241 (2007).
29. M. Fernandez-Garcia, *Catal. Rev. - Sci. Eng.* **44**, 59-121 (2002).
30. P. T. Bishop, N. A. Carthey, P. Johnston, WO 2013/008004A3, May 16, 2013.
31. R. A. Bryce, J. M. Charnock, R. A. D. Pattrick, A. R. Lennie, *J. Phys. Chem. A.* **107**, 2516-2523 (2003).
32. M. Conte *et al.*, *J. Catal.* **250**, 231-239 (2007).
33. M. Pernpointner, A.S.K. Hashmi, *J. Chem. Theory Comput.* **5**, 2717–2725 (2009).
34. A.S.K. Hashmi, *Angew. Chem. Int. Ed.* **51**, 12935 – 12936 (2012).

---

35. A. Pantelouris, G. Kiiper, J Homes, C. Feldmann, M. Jansen, *J. Am. Chem. Soc*., **117**, 11749-11753 (1995).
36. D. Tibiletti, A. Amieiro- Fonseca, R. Burch, Y. Chen, J. M. Fisher-, A. Goguet, C. Hardacre, P. Hu, D. Thompsett, *J. Phys. Chem. B,* **109**, 22553-22559 (2005)
37. G.J. Sherborne, B.N. Nguyen, *Chemistry Central Journal* , **9**, 37 (2015)
38. B. Ravel, M. Newville, *J. Synchrotron Radiat.*, **12**, 537−541 (2005)
39. M. Newville, J. Synchrotron Radiat., **8**, 322−324 (2001).
40. S. J. Clark, M. D. Segall, C. J. Pickard, P. J. Hasnip, M. J. Probert, K. Refson, M.C. Payne. *Zeitschrift fuer Kristallographie*, **220**, 567 (2005).
41. N. Govind, M. Petersen, G. Fitzgerald, D. King-Smith, J. Andzelm, *Comput. Mater. Sci.*, **28**, 250 (2003).
42. E.R. McNellis, J. Meyer, K. Reuter, *Phys. Rev. B*, **80**, 205414 (2009).
43. A. Tkatchenko, M. Scheffler, *Phys. Rev. Lett.*, **102**, 073005 (2009).
44. A.P. Seitsonen, A.M. Saitta, T. Wassmann, M. Lazzeri, F. Mauri, *Phys. Rev. B*, **82**, 115425 (2010).
45. R. Burgess, C. Buono, P.R. Davis, R.J. Davis T. Legge, A. Lai, R. Lewis, D.J. Morgan, N. Robinson, D.J. Willock, *J. Catal.*, **323**, 10 (2015).
46. H. Kitagawa, N. Kojima, T. Nakajima, *J. Chem. Soc. Dalton Trans*., 3115 (1991)
47. H. Kitagawa, N. Kojima, T. Nakajima, *J. Chem. Soc. Dalton Trans*., 3121 (1991)